Identifying and explaining vibrational modes of sanbornite (low-$BaSi_2O_5$) and $Ba_5Si_8O_{21}$: A joint experimental and theoretical study

Eduardo O. Gomes[a], Benjamin J. A. Moulton[c,d], Thiago R. Cunha[c,d], Lourdes Gracia[a,b] Paulo S. Pizani[c,d], and Juan Andrés[a*]

[a]*Departament de Química Física i Analítica, Universitat Jaume I, 12071, Castelló de la Plana, Spain*

[b]*Permanent address: Department of Physical Chemistry, University of Valencia (UV), 46100 Burjassot, Spain*

[c]*CERTEV — Center for Research, Technology, and Education in Vitreous Materials, Department of Materials Engineering, Federal University of São Carlos, 13565 - 905 São Carlos-SP, Brazil: www.certev.ufscar.br*

[d]*Universidade Federal de São Carlos, Departamento de Física, Rod. Washington Luis, Km 235 13565-905 São Carlos, SP, Brazil*

ABSTRACT

We report here the analysis of vibrational properties of the sanbornite (low-$BaSi_2O_5$) and $Ba_5Si_8O_{21}$ using theoretical and experimental approaches, as well as results of high temperature experiments up to 1100-1150˚C. The crystal parameters derived from Rietveld refinement and calculations show excellent agreement, within 4%, while the absolute mean difference between the theoretical and experimental results for the IR and Raman vibrational frequencies was <6 cm^{-1}. The temperature-dependent Raman study renders that both sanbornite and $Ba_5Si_8O_{21}$ display specific Ba and Si sites and their Ba-O and Si-O bonds. In the case of the stretching modes assigned to specific Si sites, the frequency dependence on the Si-O bond length exhibited very strong correlations. Both phases showed that for a change of 0.01 Å, the vibrational mode shifted 10 ± 2 cm^{-1}. These results are promising for using Raman spectroscopy to track *in situ* reactions under a wide variety of conditions, especially during crystallization.

Keywords: Barium silicates, sanbornite, low-$BaSi_2O_5$, $Ba_5Si_8O_{21}$, Raman spectroscopy, Rietveld refinement, DFT calculations

**Corresponding author:* J. Andrés. *E-mail address:* andres@qfa.uji.es.

1. Introduction

Barium silicates are extensively studied for their excellent material properties and device performance in a range of important technological applications [1–7] Sanbornite (low-$BaSi_2O_5$) is a uncommon mineral found in Big Creek, California (USA), and its hydrous analogue bigcreekite ($BaSi_2O_5 \cdot 4H_2O$) are rare examples where Ba is concentrated in a silicate phase [8–10]. On the other hand, $Ba_5Si_8O_{21}$ is a synthetic phase, displaying the rare characteristic of being an anhydrous phase containing ribbons (quadruple *zweier* chains) of silica tetrahedra surrounded by Ba cations which stabilize the stretched chains. Each ribbon is composed of two types of SiO_4 units that can be distinguished by the number of inter-tetrahedral linkages they contain. These can be described as Q^n species where *n* is the number oxygens bonded to adjacent Si cations. In $Ba_5Si_8O_{21}$, the tetrahedra along the edges of the ribbons are only bonded to two adjacent tetrahedra, Q^2 species, whereas the tetrahedra which form the interior of the ribbon are connected to three adjacent tetrahedra, Q^3 species. Ultimately, $Ba_5Si_8O_{21}$ is distinct from sanbornite in the presence of the Q^2 species but comparable in that ribbon and sheets are dominantly composed of Q^3 species. Both structures have been discussed in considerable detail by Liebau and colleagues [11–14].

Sanbornite and $Ba_5Si_8O_{21}$ have received considerable attention in recent years due to their desirable formation as acicular aggregates, leading to a considerable strengthening of the glass-ceramics produced and due to their high thermal expansion, which has led to their wide investigation for solid-oxide fuel cell sealant materials [5,15]. In particular, sanbornite-based glasses display volume nucleation and thus have long been of interest to researchers looking into the fundamental process of crystallization [16–22]. When doped with rare-earth elements, these materials can be used as light emitting diode materials [23,24]. Although interesting behaviors have been shown, there is a lack of clarity regarding the origin and significance of the vibrational modes and their transitions during crystallization processes [21,25–28].

Vibrational spectroscopy is one of the most versatile techniques used in the investigation of the structure of oxides and oxide glasses. For the low symmetry materials, there may be several bands calculated to lie near the position of a single observed feature. In such cases it is impossible to make an unambiguous assignment if the calculated intensities are so model-dependent that they cannot be used as an aid. Quantum-chemical computations predicting frequencies and spectral

intensities are essential to complement the interpretation of experimental spectra, particularly for complex materials where the high density of states results in spectral complexity [26].

Despite the long history of using Raman and infrared spectroscopy, as well as the employ *ab initio* quantum mechanical methods [29,30], as appropriate tools to investigate the vibrational behavior and related properties (e.g. heat capacity), few crystalline phases of silicates have had detailed determination of their vibrational modes. Early studies have been subject to the limitations and *ad hoc* assumption used to determine the dominant spectral features [29].

The temperature effect on the phonon properties of both sanbornite (low-$BaSi_2O_5$) and $Ba_5Si_8O_{21}$ is unknown yet, and it is of great interest to study their vibrational properties at high-temperature. In this context, this work investigates the vibrational modes of these systems related with the phases presented in the BaO-SiO_2 system. The experimental results are correlated with first-principle calculations, at the density functional theory (DFT) level, which allows not only the classification of the vibrational modes up to 1150˚C, but also to obtain information and structural changes undergone by these materials. The application of the described strategy allowed us to reliably describe the low-$BaSi_2O_5$ and $Ba_5Si_8O_{21}$ materials.

2. Experimental and theoretical procedures

2.1. Sample preparation

High-purity reagents, $BaCO_3$ and SiO_2 (Sigma-Aldrich, >99.9%), where used to synthesize both low-$BaSi_2O_5$ and $Ba_5Si_8O_{21}$. Due to the impurities resulting from the stable phases differing by only ~3% BaO, the solid-state reaction procedure was followed. This entails grinding the powders in a highly vibrating mill (to ensure fine and evenly distributed grain sizes) and compression into tablets and then heat-treated for 30 h at 1340 and 1410°C for low-$BaSi_2O_5$ and $Ba_5Si_8O_{21}$, respectively. Prior to heat treatment the polycrystalline tablets were calcined for 1h at 1000°C. Both phases have been confirmed by X-ray diffraction (XRD) measurements using Cu K_α radiation operating at 40 kV and a current of 20 mA in continuous scanning mode (0.5° min^{-1}) with a 2θ step of 0.02° between $10° \leq 2\theta \leq 80°$ on a Rigaku Ultima IV diffractometer. Rietveld refinement of the resulting patterns were done using the GSAS program [32,33]. A LabRAM HR800 was used to measure the Raman spectra operating a 532 nm diode laser of ~20 mW power

on the sample. Spectra where taken using a 100x visible objective, a 100 μm pinhole, an 1800 gr/mm grating resulting in a frequency and lateral spatial resolution of ~0.5 cm^{-1} and <2 μm, respectively. Spectra are the average of 12 scans of a dwell time of five seconds. Spectra have been intensity normalized to the high frequency stretching region, although raw spectra have roughly equal intensity. Measured Raman active modes were curve fit using Lorentzian lineshapes to determine individual peak parameters. High temperature measurements were carried out on 40-60 mg polycrystalline monolithic chips heated using a Linkam stage and a 50x SLWD objective. Slightly longer spectra (10 second dwell time and 16 spectra were averaged) were taken as the furnace window cuts the measured intensity to roughly a third of ambient condition spectra.

2.2. Computational methods

DFT calculations of the lattice parameters and vibrational modes were done using Becke's three-parameter hybrid non-local exchange functional, combined with a Lee-Yang-Parr gradient-corrected correlation functional (B3LYP), implemented in the CRYSTAL17 package [34]. The atoms were centered and described using pseudopotential databases; [35], 88-31G* [36] and 8-411d11G [37] (all-electron) for Ba, Si and O, respectively. Regarding the diagonalization of the density matrix, the reciprocal space net was described by a shrinking factor of 4, generated according to the Monkhorst–Pack scheme. The accuracy of the evaluation of the Coulomb and exchange series was controlled by five thresholds, whose adopted values were 10^{-7}, 10^{-7}, 10^{-7}, 10^{-7}, and 10^{-14}. The vibrational frequencies calculation was performed at the Γ point within the harmonic approximation, and the dynamic matrix was computed by the numerical evaluation of the first derivative of analytical atomic gradients.

3. Results and discussion

3.1. XRD analysis

The XRD patterns of the synthesized samples are shown in Fig. 1. The crystal structure parameters are in agreement with the literature results, Table 1. The Rietveld refinement results are comparable to published results having a goodness-of-fit (χ^2) close to unity and R values below 10% [38]. The cell volumes for the measured and calculated structures of low-$BaSi_2O_5$ and $Ba_5Si_8O_{21}$ are less than 1% and 4% of the published values [11,12,15], respectively. Therefore, the simulations show a very good agreement with the experimental results of the measured structures.

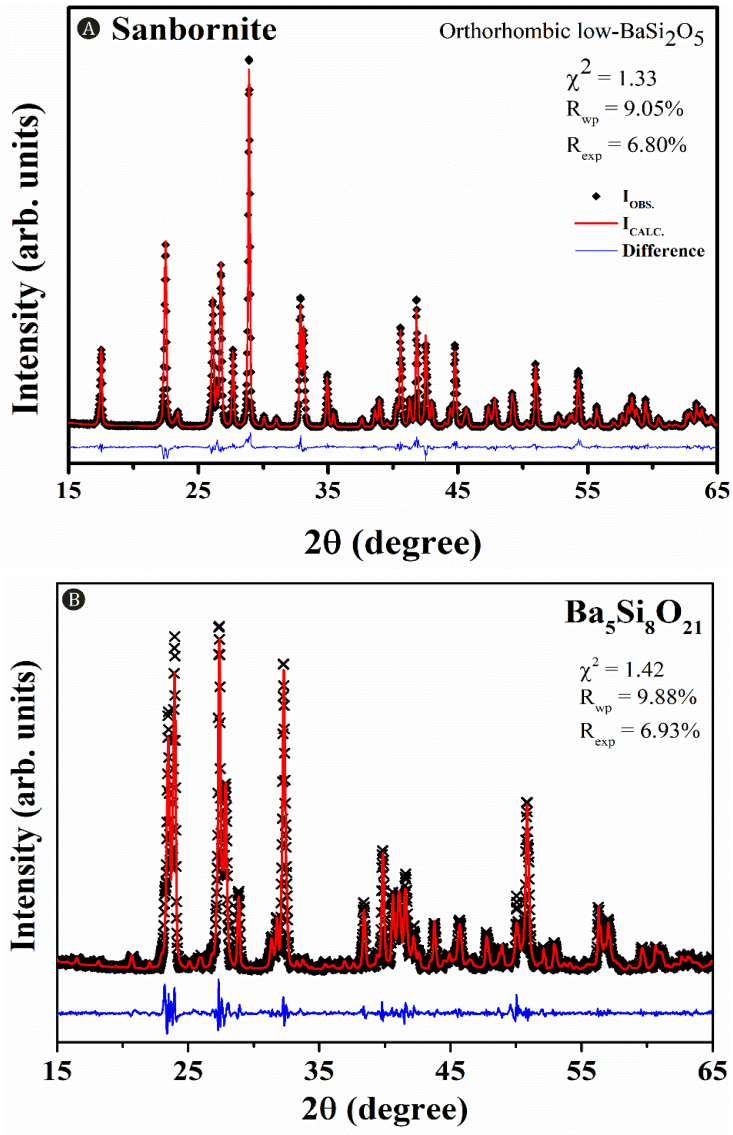

Figure 1: Rietveld refinement of diffraction patterns for A) sanbornite and B) $Ba_5Si_8O_{21}$.

Table 1: Crystal structural parameters of barium silicate phases in this study.

Phase	Formula	Space Group	Density[1] (g/cm^3)		Cell Volume	a	b	c	β	Reference
			theoretical	experimental	($Å^3$)	(Å)	(Å)	(Å)	(degrees)	
Sanbornite low-$BaSi_2O_5$	$BaSi_2O_5$	Pmcn	3.77	3.70	481.25	7.688	4.629	13.523	90.00	[12]
					481.78	7.690	4.632	13.528	90.00	[15]
					483.02	7.696	4.636	13.538	90.00	This study - Rietveld
			3.632		500.84	7.778	4.684	13.744	90.00	This study - DFT
B5S8	$Ba_5Si_8O_{21}$	C2/c	3.925	3.93	2110.20	32.675	4.695	13.894	98.10	[11]
					2120.6	32.739	4.702	13.917	98.17	[15]
					2121.6	32.756	4.705	13.909	98.18	This study - Rietveld
			3.771		2200.3	33.284	4.738	14.097	98.29	This study - DFT

[1] reported in [13].

Sanbornite is a phyllosilicate composed of two layers: one of Q^3 species and one of BaO_9 polyhedra (Figure 2). Each of the Q^3 species are connected to adjacent tetrahedra *via* bridging oxygens (BO) at the O1 and O3 sites whereas the O2 oxygen is a non-bridging oxygen (NBO) which is only bonded to one Si and three Ba atoms. Topologically, sanbornite can be described as a 6^3 net or an infinite layer of six-membered tetrahedral rings [39]. The large size of the Ba cations distorts each sheet such that the NBO are sticking out towards the Ba cations. This results in a relationship between the layers were one BaO_9 polyhedron sits atop of two silica tetrahedra, and vice versa.

Table 2: Experimental and calculated vibrational modes in sanbornite.

Mode	Infrared modes			Raman modes						
	Frequency cm^{-1}	Symmetry	Origin	Frequency cm^{-1}	FWHM cm^{-1}	Relative Intensity (%)	Frequency cm^{-1}	Symmetry	Δν	Origin[3]
ν_1	60.0	A_u	lattice	55.0	1.2	11	59.8	A_g	-4.8	O2-Ba
ν_2	66.1	B_{2u}	O2-Ba	70.1	3.5	14	71.5	B_{2g}	-1.4	Ba-O2-Si
ν_3	75.9	A_u	Ba-O2-Si	71.9	2.2	34	78.0	B_{3g}	-6.1	Ba-O2
ν_4				93.0	2.2	14	78.3	B_{1g}	14.7	SiO4
ν_5				98.6	1.8	1	99.5	A_g	-0.9	Ba-O2
ν_6	104.4	B_{1u}	Ba-O2	103.3	2.4	4	102.3	B_{3g}	1.0	lattice
ν_7							110.1	A_g		Ba-O2-Si
ν_8	120.3	B_{3u}	lattice				116.4	B_{2g}		Ba-O2
ν_9	126.3	B_{1u}	Si-O2	118.2	3.0	23	118.5	B_{1g}	-0.3	lattice
ν_{10}	134.9	B_{2u}	O1-Si-O2	122.0	6.7	6	125.1	B_{3g}	-3.1	Si-O2
ν_{11}	135.8	B_{3u}	lattice				126.8	A_g		O1-Si-O3
ν_{12}	137.5	B_{1u}	O1-Si-O3	148.5	6.0	3	159.6	B_{2g}	-11.1	Ba-O2
ν_{13}	182.5	B_{2u}	lattice	168.8	7.4	2	182.7	B_{3g}	-13.9	Si-O2
ν_{14}	198.7	A_u	Ba-O2	191.5	7.9	16	203.0	B_{1g}	-11.5	Ba-O2
ν_{15}	209.3	A_u	Ba-O2	224.0	10.4	19	216.9	A_g	7.1	Si-O3
ν_{16}	212.8	B_{1u}	lattice	247.4	6.0	6	236.3	B_{1g}	11.1	lattice
ν_{17}	253.8	B_{2u}	Ba-O2	267.4	7.2	5	259.9	B_{3g}	7.5	lattice
ν_{18}	259.3	B_{3u}	lattice				278.0	B_{2g}		Ba-O2,3-Si
ν_{19}	294.6	B_{1u}	Si-O2	292.3	12.6	5	299.3	A_g	-7.0	lattice
ν_{20}	312.8	B_{2u}	Si-O1-Si	315.7	5.0	11	322.2	B_{3g}	-6.5	Ba-O2
ν_{21}	325.5	B_{3u}	lattice	332.6	3.8	17	330.6	B_{1g}	2.0	O3-Si-O1
ν_{22}	327.6	A_u	O3-Si-O1	341.8	4.6	11	342.2	B_{2g}	-0.4	lattice
ν_{23}	372.0	B_{1u}	Ba-O2				355.3	A_g		Ba-O2
ν_{24}	389.1	A_u	O2-Si-O3				391.9	B_{3g}		lattice
ν_{25}	401.7	B_{2u}	lattice	386.1	5.2	3	392.9	B_{1g}	-6.8	O2-Si-O3
ν_{26}	438.9	B_{2u}	O1-Si-O2	431.5	6.3	0	438.6	B_{3g}	-7.1	O1-Si-O2
ν_{27}	453.9	B_{3u}	O3-Si-O1	453.0	3.2	1	457.0	B_{2g}	-4.1	SiO_4
ν_{28}	468.4	B_{1u}	O1-Si-O3	459.0	6.1	2	464.6	A_g	-5.6	O1-Si-O3
ν_{29}	473.1	A_u	O2,3-Si-O3	476.2	2.7	8	479.3	B_{1g}	-3.1	O2,3-Si-O3
ν_{30}	486.3	B_{1u}	O1-Si-O3	492.8	2.8	1	488.2	A_g	4.6	O1-Si-O3
ν_{31}	507.5	B_{3u}	O3-Si-O2				508.4	B_{2g}		O3-Si-O2
ν_{32}	535.6	B_{1u}	O3-Si-O2	535.5	8.2	66	534.5	A_g	1.0	O3-Si-O2
ν_{33}	538.7	B_{2u}	SiO_4				550.0	B_{3g}		SiO_4
ν_{34}	594.1	A_u	O3-Si-O2	597.2	5.9	7	594.4	B_{1g}	2.8	O3-Si-O2
ν_{35}	693.6	B_{2u}	Si-O1				703.8	B_{3g}		SiO_4
ν_{36}	758.8	B_{3u}	Si-O3				759.7	B_{2g}		O3-Si
ν_{37}	773.1	B_{1u}	SiO_4	756.5	9.4	1	760.6	A_g	4.1	SiO_4
ν_{38}	803.5	B_{2u}	Si-O3-Si				805.9	B_{3g}		Si-O3-Si
ν_{39}	971.1	B_{3u}	SiO_4				973.2	B_{1g}		O2,3-Si
ν_{40}	972.4	A_u	O3-Si-O2				973.6	B_{2g}		SiO_4
ν_{41}	980.5	B_{1u}	O3-Si-O2	986.6	9.6	2	980.4	A_g	6.2	O3-Si-O2
ν_{42}	1001.4	B_{3u}	O1-Si	1000.3	5.2	2	1004.1	B_{2g}	-3.7	O1-Si
ν_{43}	1035.6	A_u	SiO_4	1037.4	3.8	1	1046.1	B_{3g}	-8.7	O2,3-Si
ν_{44}	1047.7	B_{2u}	O2-Si				1053.4	B_{1g}		O2-Si
ν_{45}	1084.3	A_u	O1-Si	1077.9	4.5	100	1084.5	B_{1g}	-6.6	O1-Si
ν_{46}	1095.1	B_{3u}	SiO_4	1100.1	4.9	1	1096.3	A_g	3.8	O2-Si
ν_{47}	1095.3	B_{2u}	O3-Si				1113.2	B_{2g}		O1,2-Si
ν_{48}	1100.6	B_{1u}	O2-Si	1172.9	10.3	1	1193.0	B_{3g}	-20.1	O3-Si
				Mean A_g FWHM[1]	7.8			$\lvert\Delta\nu\rvert$[2]	5.8	
				Mean B_g FWHM[1]	5.3			max. Δν	20.1	

[1] only modes contributing >1% to the area were considered.

[2] $|\Delta\nu|$ is the absolute mean difference between theoretical and experimental frequency.

[3] Note O1 & O3 are BOs whereas O2 is a NBO (Fig. 2).

168

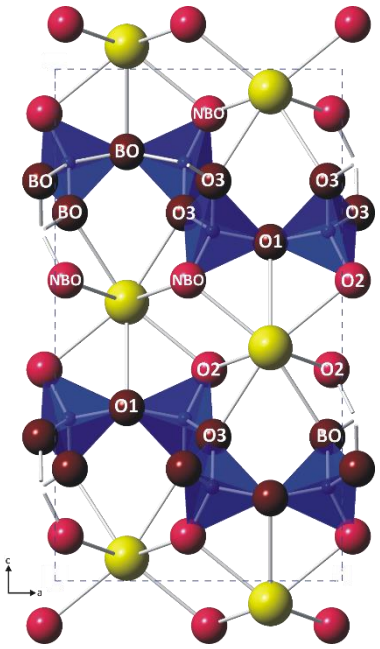

Figure 2: A schematic representation of the sanbornite crystal structure. Ba are large yellow spheres (colour online). Blue Si-centered tetrahedra show dark red BO and lighter pink NBO. Site labels refer to those in table 2. The directions defined by the a and c lattice parameters are drawn.

169 $Ba_5Si_8O_{21}$ has 18 crystallographic sites (Figure 3) and as a consequence has a large number
170 of Raman modes (Table 3). This phase is a rare silicate composed of quadruple zweier chains that
171 form ribbons that can be described topologically as $^2T_2{}^3T_6$ ribbons [40]. In the $Ba_5Si_8O_{21}$ structure,
172 the edge of each ribbon has Q^2 species at the Si1 site. The remaining Si sites (Si2-Si4) are Q^3
173 species, all of which have three BO and one NBO. The Q^n species display distinct vibrational
174 frequencies.

175

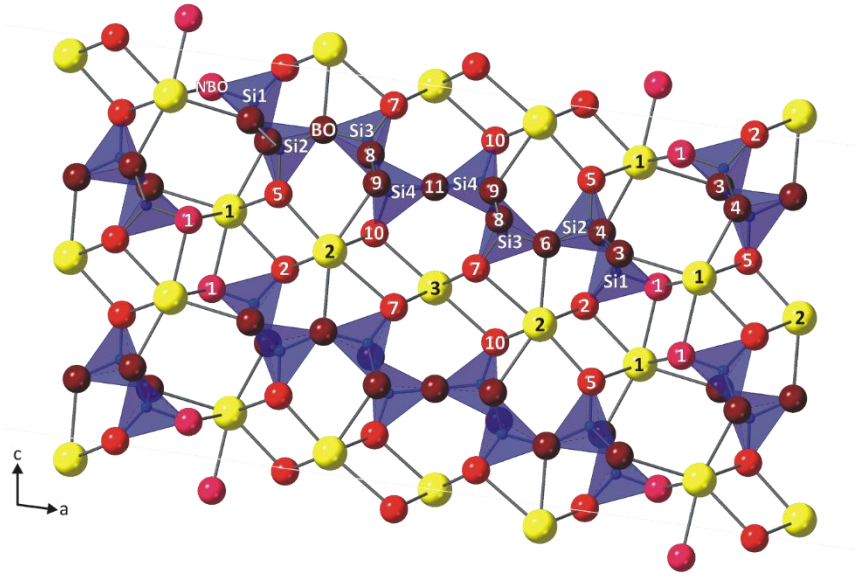

Figure 3: A schematic representation of the unit cell showing structural features of $Ba_5Si_8O_{21}$. Site labels refer to those in Table 3 and colors follow those in figure 2. The directions defined by the a and c lattice parameters are drawn.

Table 3: Experimental and theoretical vibrational modes in $Ba_5Si_8O_{21}$*

Mode	Infrared modes			Raman Modes						
	Frequency cm^{-1}	Symmetry	Origin[2]	Frequency cm^{-1}	FWHM cm^{-1}	Relative Intensity (%)	Area %	Frequency cm^{-1}	Symmetry	Δν	Origin[1]
ν_1	-69.5	B_u	O10-Si4					-53.7	B_g		O10-Si4
ν_1	45.9	A_u	O2-Ba2-O10	51.8	3.2	5	<1	54.5	A_g	2.7	lattice
ν_2	55.5	B_u	Ba2-O1-Si1	57.1	1.8	6	<1	55.7	B_g	-1.4	O10-Ba2-O2,O6
ν_3	62.5	A_u	O5-Ba2-O7	59.9	2.1	4	<1	60.1	A_g	0.2	O6-Ba2-O10
ν_4	64.7	B_u	O2-Ba2-O5,6	65.4	2.9	19	1.2	73.0	B_g	7.6	Ba2-O6-Si3
ν_5	68.3	A_u	O4-Ba1-O2								
ν_6	70.2	B_u	O10-Ba3-O7	71.6	0.8	2	<<1	74.2	A_g	2.6	lattice
ν_7	73.2	B_u	O1-Ba1-O4,5								
ν_8	75.3	A_u	Ba2	76.8	4.2	15	1.3	80.2	B_g	3.4	O5-Ba1-Si1/O1
ν_9	81.4	A_u	Ba3-O10-Si4	81.8	4.0	23	2.0	85.9	A_g	4.1	lattice
ν_{10}	87.8	B_u	Ba3-O7-Si3	85.3	4.1	9	<1	87.7	B_g	2.4	lattice
ν_{11}	88.6	A_u	O2-Ba1-O4-Ba2-O10-Ba3	88.9	5.1	15	1.7	93.4	A_g	4.5	complex
ν_{12}	99.4	B_u	Ba3-O7	92.6	4.8	23	2.4	98.0	B_g	5.4	O1-Ba1-O2,5
ν_{13}	101.1	A_u	O2,5-Ba1-O1	98.3	5.6	9	1.0	101.7	B_g	3.4	Ba2-various O
ν_{14}	104.4	A_u	Ba lattice	102.5	3.9	19	1.6	101.8	A_g	-0.6	Si1-O2-Ba1,2-O10
ν_{15}	108.0	B_u	Ba1,3-various O-Si1	105.3	6.5	30	4.2	105.8	B_g	0.5	O1,4-Ba1-O2/Si1
ν_{16}	112.4	B_u	Ba2-O10-Ba3					106.0	A_g		Ba1-Si1 lattice
ν_{17}	114.0	B_u	Ba3-O7	114.4	8.2	8	1.4	115.5	B_g	1.1	Ba2-O10-Ba3
ν_{18}	115.1	A_u	Ba3-O7,10 & Si4-O11					117.2	A_g		O4-Ba1-O1
ν_{19}	118.6	A_u	O4-Ba1-O1	122.8	1.0	1	<<1	122.9	A_g	0.1	Si4-O11
ν_{20}	122.3	B_u	O10-Ba2-O2 & O10-Ba3-O7					133.8	B_g		Ba2-O10-Si4 & O7-Ba3-O10
ν_{21}	125.1	A_u	O5-Ba2-O10 & Si4-O11	132.8	6.0	9	1.2	134.0	A_g	1.2	O10-Ba2-O6
ν_{22}	130.1	A_u	O7-Ba3 & O10-Ba3	140.6	10.4	2	<1	141.6	B_g	1.0	O6-Ba2-O10-Ba3
ν_{23}	138.3	B_u	O7,10-Ba3 &O10-Ba3					143.6	A_g		lattice
ν_{24}	139.6	A_u	lattice	149.2	4.1	3	<1	154.4	B_g	5.2	lattice
ν_{25}	155.9	B_u	lattice	164.6	7.3	4	<1	160.9	A_g	-3.7	O1-Ba1-O2 & O5-Ba2
ν_{26}	166.4	A_u	lattice	168.6	9.2	9	1.8	167.7	B_g	-0.9	O4-Ba1-O2
ν_{27}	166.6	B_u	O4-Ba1-O2	186.0	10.5	7	1.6	176.8	A_g	-9.2	O1,5-Ba1,2
ν_{28}	188.5	A_u	Ba1,2 lattice	196.0	11.9	2	<1	196.2	B_g	0.2	lattice
ν_{29}	196.0	B_u	O5,6-Ba1,2-O1,2,6	209.1	8.6	6	1.0	208.1	A_g	-0.9	O1,4-Ba1,2-O1,2,5
ν_{30}	204.4	A_u	O4-B1-O2 & O4-Si2-O6					209.2	B_g		O1-Ba1-O4
ν_{31}	212.8	B_u	O2-Ba1-O1					217.7	B_g		O2-Ba1,2-O1,5
ν_{32}	217.7	B_u	O2-Ba1,2-O1,5					226.7	A_g		O1-Ba1 & O3-Si1-O4
ν_{33}	221.1	A_u	O2-Ba1 & O2-Ba2-O5					227.7	B_g		lattice
ν_{34}	229.4	A_u	lattice	241.5	12.8	30	8.4	233.1	A_g	-8.4	O2-Ba1 & O2,6-Ba2-O2,5
ν_{35}	233.7	B_u	lattice					250.8	A_g		O5-Ba1,2-O1,2
ν_{36}	243.2	B_u	lattice	257.7	10.0	15	3.2	255.1	B_g	-2.6	O5-Ba1,2-O1,10
ν_{37}	259.6	A_u	lattice					264.7	A_g		lattice
ν_{38}	266.6	B_u	lattice	273.6	9.8	16	3.5	274.5	B_g	0.9	lattice
ν_{39}	269.5	A_u	lattice	283.7	9.0	37	7.2	280.7	A_g	-3.0	lattice
ν_{40}	279.3	B_u	O7,10-Ba2,3-O2,7	297.8	8.3	6	1.0	299.6	B_g	1.9	O10-Ba2,3-O2,7
ν_{41}	290.8	A_u	lattice	306.6	9.7	8	1.8	300.4	A_g	-6.2	lattice
ν_{42}	296.4	A_u	O10-Ba2-O2 & Ba3-O7,10	316.3	8.9	9	1.7	310.6	B_g	-5.6	O2,5-Ba1,2-O1,5,10
ν_{43}	303.2	B_u	O1-Ba1,2-O1,5	324.8	5.8	3	<1	322.1	A_g	-2.7	Ba1,3-O1,5,7
ν_{44}	314.5	A_u	O7-Ba3-O10					322.2	B_g		Ba3-Si3-O7,9,10
ν_{45}	321.7	B_u	O9-Si3,4-O6,11					332.5	B_g		O1-Ba1-O5-Si1
ν_{46}	324.3	A_u	Ba2,3-O2,7,10					333.9	A_g		lattice
ν_{47}	330.4	B_u	all Ba rattle					350.0	A_g		lattice
ν_{48}	338.1	A_u	Ba2,3-O10-Si4	363.1	8.2	3	<1	361.7	A_g	-1.4	lattice
ν_{49}	359.5	A_u	lattice	375.2	8.4	4	<1	369.2	B_g	-6.0	lattice
ν_{50}	372.3	B_u	lattice					384.7	B_g		O11-Si4-O10
ν_{51}	381.1	A_u	O8-Si3-O7 & Si4-O11	393.7	9.8	2	<1	386.2	A_g	-7.5	Si4-O11
ν_{52}	383.1	B_u	O11-Si4-O10					400.1	B_g		O5-Si2-O6
ν_{53}	393.8	B_u	O5-Si2-O6	409.2	6.3	3	<1	406.8	A_g	-2.4	lattice
ν_{54}	413.5	A_u	O5-Si2-O4	430.4	5.4	4	<1	421.5	B_g	-8.9	O10-Si4-O11
ν_{55}	420.6	B_u	O10-Si4-O11								
ν_{56}	433.5	A_u	lattice	439.0	4.6	5	<1	444.9	A_g	5.9	O1-Si1-O2
ν_{57}	457.2	B_u	Si1-O1-Ba1	445.0	5.6	5	<1	451.1	B_g	6.1	O1-Si1-O2 & O10-Si4-O8
ν_{58}	463.9	A_u	Si4-O10-Ba2	449.4	6.3	4	<1	465.4	B_g	16.0	O4-Si1-O1
ν_{59}	464.0	B_u	O4-Si1-O1	468.6	4.6	11	1.1	467.4	A_g	-1.2	Si4-O10-Ba2
ν_{60}	481.4	B_u	O11-Si4-O8	471.0	6.2	6	<1	484.2	A_g	13.2	O1-Si1-O4 & O3-Si2-O5
ν_{61}	485.8	A_u	O3-Si2-O5	480.9	5.6	14	1.7	484.7	B_g	3.8	Si3-O8-Si4 & O11-Si4-O8
ν_{62}	490.8	A_u	O1-Si1-O4	501.8	8.1	22	3.9	488.7	A_g	-13.1	Si3-O6-Ba2
ν_{63}	498.4	B_u	O2-Si1-O4 & Si3-O6-Ba2	506.7	4.4	10	1.0	494.9	B_g	-11.8	O2-Si1-O2
ν_{64}	511.6	A_u	Si4-O8-Si3	516.7	3.8	3	<1	512.9	A_g	-3.8	Si4-O8-Si3
ν_{65}	522.7	B_u	Si1-O3-Si2 & O9-Si3-O6	523.6	4.7	14	1.5	523.9	B_g	0.2	Si1-O3-Si2 & O8-Si3-O9
ν_{66}	532.5	A_u	O8-Si4-O10	535.1	5.3	88	12.6	536.1	A_g	1.0	O7,9-Si3,4
ν_{67}	539.9	B_u	Si3,4-O8,9					545.0	B_g		Si3-O9-Si4
ν_{68}	540.7	A_u	Si3-O9-Si4	545.7	5.3	50	5.8	545.5	A_g	-0.2	O7-Si2-O5 & O9-Si3-O8
ν_{69}	555.4	B_u	O3-Si2-O4					555.6	B_g		O3,4-Si2-O5,6
ν_{70}	562.0	A_u	O4-Si1-Ba1 & O3-Si2-O4					564.5	A_g		O4-Si1-Ba1
ν_{71}	589.3	B_u	O4-Si1-O3	601.9	6.7	24	3.5	587.7	B_g	-14.3	O4-Si1-O3
ν_{72}	633.3	B_u	Si rattle	613.9	7.3	22	3.5	626.4	A_g	12.5	Si1-O4-Si2
ν_{73}	634.5	A_u	Si1-O4-Si2	632.1	6.5	3	<1	639.2	B_g	7.1	Si1-O4-Si2
ν_{74}	717.1	A_u	O8,10-Si4-O11					717.6	A_g		O8,10-Si4-O11
ν_{75}	735.6	B_u	Si1-O3,6-Si2					734.5	B_g		Si1-O3,6-Si2
ν_{76}	738.1	A_u	O3-Si1-Ba1	736.1	6.7	1	<1	739.6	A_g	3.5	O3-Si1-Ba1
ν_{77}	753.2	B_u	O4-Si2-O5	749.2	10.2	20	4.4	757.4	A_g	8.2	Si2-O4-Ba1 & O6-Si2-O3
ν_{78}	759.0	A_u	O4-Si2-O5					759.4	B_g		Si2-O4-Si1
ν_{79}	770.6	B_u	Si3-O8,9-Si4					774.2	A_g		Si3-O8,9-Si4
ν_{80}	781.6	A_u	Si3-O8,9-Si4					779.4	B_g		Si3-O8,9-Si4
ν_{81}	924.3	B_u	O3,4-Si2					925.3	B_g		O3,4-Si2
ν_{82}	924.4	A_u	O3,4-Si2	920.7	4.8	16	1.6	926.0	A_g	5.3	O3,4-Si2
ν_{83}	937.0	B_u	O2-Si1	924.0	7.2	32	5.1	934.1	A_g	10.1	O1,2-Si1
ν_{84}	941.9	A_u	O1-Si1					952.8	B_g		O1,2-Si1
ν_{85}	965.5	B_u	Si3-O9-Si4 & O9-Si4					966.2	B_g		Si3-O9-Si4 & O9-Si4
ν_{86}	966.5	A_u	Si3-O9-Si4 & O9-Si4	969.7	12.4	2	<1	967.2	A_g	-2.5	Si3-O9-Si4 & O9-Si4
ν_{87}	978.4	B_u	O8-Si3-O6, O8-Si4-O10	987.5	2.9	0	<<1	986.0	B_g	-1.4	O8-Si3-O6
ν_{88}	997.1	A_u	O4-Si1 & O7-Si3	1004.0	7.3	3	<1	1011.5	B_g	7.5	O6-Si2 & O10-Si4
ν_{89}	1008.4	B_u	O6-Si2 & O10-Si4	1011.3	4.7	13	1.3	1012.6	A_g	1.2	O1-Si1-O2
ν_{90}	1016.3	A_u	O2-Si1	1024.4	3.8	11	<1	1018.2	A_g	-6.1	O3,4-Si1-Ba1 & O7-Si3
ν_{91}	1023.7	A_u	O6-Si2 & O10-Si4	1027.6	8.6	14	2.6	1021.8	B_g	-5.8	O1,O2-Si1
ν_{92}	1028.4	B_u	O2-Si1					1042.8	A_g		O1-Si1
ν_{93}	1046.5	B_u	O1-Si1 & O7-Si3	1053.5	7.4	7	1.2	1045.5	B_g	-8.0	Si2-O6-Ba2 & O6,7-Si3
ν_{94}	1056.9	B_u	O6,7-Si3	1066.8	5.5	100	12.1	1064.7	B_g	-2.1	O7-Si3
ν_{95}	1064.5	A_u	O6-Si3	1069.6	5.7	44	5.5	1065.1	A_g	-4.5	O5-Si2
ν_{96}	1075.8	B_u	O3,5,-Si2 & O8-Si4	1075.3	4.5	64	6.3	1078.6	A_g	3.3	O8,10-Si4
ν_{97}	1078.0	A_u	O3,5-Si2 & O8-Si4					1085.6	A_g		O7-Si2
ν_{98}	1086.0	A_u	O7-Si3	1094.1	3.3	1	<<1	1107.6	B_g	13.5	Si1-O4-Si2
ν_{99}	1089.0	B_u	O5-Si2-O6	1099.4	5.2	1	<<1	1108.8	A_g	9.4	Si2-O6-Si3
ν_{100}	1129.5	A_u	Si4-O5,8	1130.4	8.4	0	<<1	1132.4	B_g	2.0	Si4-O11
ν_{101}	1178.8	B_u	Si4-O11	1171.1	11.0	1	<1	1197.9	B_g	26.8	Si4-O11
				Mean A_g FWHM	6.9						
				Mean B_g FWHM	7.0						
										max. Δν	26.8

										|Δν|	5.1

* the symbols used are the same as in table 2.

[1]- Note O1, O2, O5, O7 & O10 are NBO whereas O3, O4, O6, O8, O9 and O11 are BO. Si1 is the Q^2 whereas Si2-Si4 are Q^3 species (see Fig. 3).

3.2. Vibrational modes

3.2.1. Low-$BaSi_2O_5$

The primitive cell of sanbornite (*Pmcn*) contains 32 atoms and therefore, 96 normal modes including the three acoustic translations (B_{1u}, B_{2u} & B_{3u}) (Figure 2). The correlation method [41] allows for the determination of the vibrational modes at the center of the Brillouin zone, $\Gamma_{vibrational}^{L-BaSi2O5} = 13A_g^R + 11B_{1g}^R + 11B_{2g}^R + 13B_{3g}^R + 11A_u^{silent} + 12B_{1u}^{IR} + 12B_{2u}^{IR} + 10B_{3u}^{IR}$. There is no known published evaluation of the vibrational spectra despite the multiple Raman studies involving sanbornite [27,28,42]. However, theoretical results reproduce the experimental vibrational modes with an absolute mean deviation of <6 cm^{-1}, and the high degree of overlap in the measured peaks and the displacement from unity in the calculated frequencies yields a small potential for ambiguity. For example, the measured modes numbering 12 (148.5 cm^{-1}) through 17 (267 cm^{-1}) *could* correspond to the calculated modes at 182.7 through 278.0 cm^{-1}. The overall agreement found between measured and simulated frequencies suggests that the spectrum can be divided into four regions according to the predominant symmetry character of the modes: the essentially rigid rotational motions occur below 100 cm^{-1}; bending modes involving Ba-O polyhedral from 100-400 cm^{-1}; intra- or inter-tetrahedral bending modes (O-Si-O, Si-O-Si), with varying degree of Ba participation, at the range 400-760 cm^{-1}; the stretching mode region found >800 cm^{-1}. However, there are several stretching modes around 118 and 160 cm^{-1} and bending modes in the stretching region. Modes described as *lattice* involve significant movement of both the BaO_9 and SiO_4 sublattices. The complete list of mode symmetries and cations involved are reported in Table 2.

An analysis of the theoretical results of Table 2 shows that there is no distinction in either the relative intensities, the linewidths, or symmetry of modes involving a particular site (whether Si or Ba). Apart from the frequency distinctions there is no physically measurable parameter that distinguishes modes involving Si from Ba, nor distinguishing BO from NBO behavior.

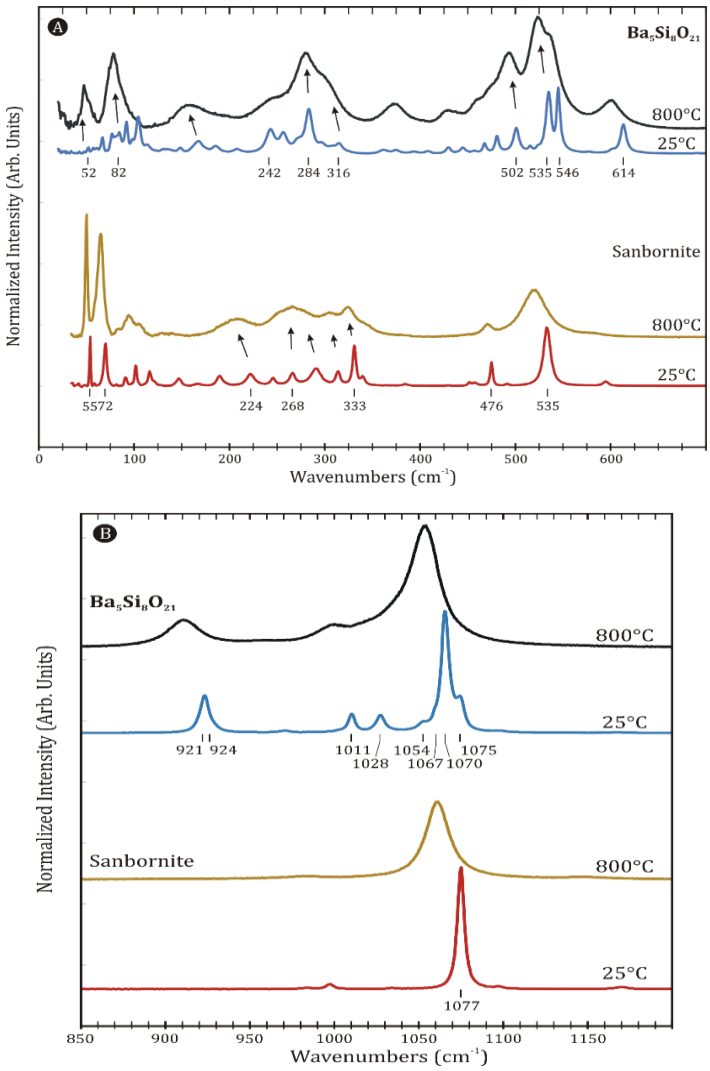

Figure 5: Spectra of sanbornite and $Ba_5Si_8O_{21}$ at 25ªC and 800 ºC. A) the low frequency region and B) the high frequency stretching modes. Arrows highlight the vibrational modes.

The primitive cell of $Ba_5Si_8O_{21}$ (*C2/c*) contains 68 atoms and consequently 204 normal modes including the acoustic modes ($A_u + 2B_u$). The vibrational modes at Brillouin zone center can be composed as: $\Gamma_{vibratinal}^{Ba5Si8O21} = 49A_g^R + 50B_g^R + 51A_u^{IR} + 51B_u^{IR}$. The theoretical results reproduce the experimental observed modes slightly better than for sanbornite with a lower absolute mean deviation of <5.1 cm^{-1}. It is important to remark that numerous vibrational modes leave some ambiguity, especially at lower frequencies where many modes overlap. Note that the Ba3 and O11 sites (Figure 3) are found at the Wycoff sites 4a and 4e, respectively, and consequently, the correlation method would infer that the Ba3 is not Raman active and that O11

site would only contribute to three modes. Fortunately, our simulation shows that this inference is somewhat misleading. An analysis of the results of Table 3 renders that the Ba3 site contributes to at least six modes whereas the O11 site contributes to multiple modes included several pure Si4-O11 stretching modes with values larger than 1100 cm^{-1}. This result highlights the necessity of *ab initio* simulations in determining the origin of the Raman modes. As with sanbornite, the spectra can be divided into four regions with small shifts in the limits (Figure 4). The essentially rigid rotational motions occur below 100 cm^{-1}; bending modes involving Ba-O polyhedral from 100-370 cm^{-1}; intra- or inter-tetrahedral bending modes (O-Si-O, Si-O-Si), with varying degree of Ba participation, found from 370-780 cm^{-1}; the stretching mode region found >900 cm^{-1}.

The same caveats noted above apply to our analysis of $Ba_5Si_8O_{21}$, however, given the complexity of the spectra we emphasize that the agreement is excellent. The above modes are discussed in more detail below along with some correlations to their crystal chemical properties.

Table 4: Values of thermal effects on the mode parameters for sanbornite.

Mode	Center (C)		Shift	Linewidth[1]		% of Variance[2]		γ_P[3]
	ν_0	T_{max}	$10^3\ \delta\nu/\delta T$	W_0	$10^3\ \delta W/\delta T$	v	W	
ν_1	55.0	1150	-6.5	0.9	1.7	h	m	3.22
ν_3	71.9	1150	-8.6	3.0	4.5	h	h	3.26
ν_6	103.3	1150	-9.9	3.9	4.8	h	l	2.61
ν_9	118.2	1150	-13.5	4	n.d.	h		3.11
ν_{12}	148.5	925	-20.6	5	n.d.	h		3.78
ν_{15}	224.0	1150	-11.4	12.5	14.7	m	m	1.39
ν_{16}	247.4	1150	3.4	4.1	24.6	l	h	-0.37
ν_{17}	267.4	1150	-2.3	8.2	15.7	l	h	0.23
ν_{19}	292.3	1150	-11.3	13	n.d.	h		1.05
ν_{20}	315.7	1150	-13.3	4.6	19.8	h	h	1.15
ν_{21}	332.6	1150	-10.0	2.8	17.9	h	vh	0.82
ν_{22}	341.8	1150	2.9	4.3	14.4	m	h	-0.23
ν_{29}*	476.2	1150	-7.2	3.0	7.7	h	h	0.41
ν_{32}	535.5	1150	-19.0	8.7	26.6	h	vh	0.97
ν_{34}	597.2	1150	-30.0	9.7	10.8	m	l	1.37
ν_{37}	756.5	1150	-20.8	12.2	9.9	h	l	0.75
ν_{42}	1000.3	1150	-25.8	n.d.				0.70
ν_{45}	1077.9	1150	-19.7	2.8	18.4	h	h	0.50
ν_{48}	1172.9	1150	-31.7	20-40	n.d.	h		0.74

* FWHM deviates from linearity around 800˚C

[1] W = full-width at half-maximum; n.d. = not determined

[2] % of variance explained by regression model: v = very; h = high, R^2>0.9; m = moderate, R^2>0.75; l = low, R^2>0.5

[3] $\gamma_P = (-1/\alpha\nu_0)(\delta\nu/\delta T)_P$, where α is the room temperature volume expansion coefficient (3.67×10^{-5}/K) determined from the structural data of [15].

3.3. Temperature dependence of Raman modes

In general, as temperature increases, a thermal expansion takes place with concomitant increase of the crystal volume by lengthening bonds and increasing the inter-tetrahedral angles. These changes should be recorded in the frequencies of the vibrational modes. Twenty of the 33 measured modes found for sanbornite (Table 2) have been consistently identified up to 1150˚C, and therefore, can be related to its thermal expansion. Table 4 includes the ambient position center (ν_0) and linewidth (W_0) and their temperature dependences ($\delta\nu/\delta T$ and $\delta W/\delta T$, respectively) as well as a confidence indicator whether regression well ($R^2 > 0.9$) to weakly describes the mode trend. Modes not included in this table were not well constrained or too weak to follow as the temperature increases.

Raman modes are related to specific bonds, and/or groups of bonds, that can be characterized by their crystal chemical properties. For instance, the Ba-O2 bonds are solely responsible for

vibrational modes at 55.0, 71.9, 148.5, and 315.7 cm^{-1}, however, not all are well defined. Using the thermal expansion data of Gorelova et al., [15], combined with our *in situ* high temperature data reported here allows us to determine the mode dependence on various crystal structure parameters.

In Figure 4, representative spectra at room temperature and 800˚C were chosen to show the temperature dependence of the modes. At higher temperatures, >800˚C, the distinctions between overlapping modes are lost due to homogeneous broadening. The vibrational modes with very low values of frequency at 55.0 (ν_1) and 71.9 cm^{-1} (ν_3) are well defined, and become increasingly so, at higher temperatures (Figure 4a). The low frequency bands are related to rigid motions of the Ba-O2 bonds and, therefore relate directly to the bond length and indirectly to the volume of the BaO_9 polyhedron (Figure 5). Although they both have slightly different dependencies, they are similar at roughly ~1.5 cm^{-1} for bond length change of 0.01 Å (Fig. 6a). A difference quite easily measured given the resolution of our Raman spectrometer. Likewise, the 1077.9 cm^{-1} (ν_{45}) stretching mode of the O1 away from the central Si atom shows an even stronger correlation with the bond length (Fig. 6c). This stretching mode is much more sensitive to a changing bond length in that for every 0.01 Å the frequency shifts by -9.8 cm^{-1}. This bond length shift is very similar but even more strongly correlated than that found for the Si-O stretching modes and bond lengths in forsterite (Mg_2SiO_4) [30]. Another intense mode is found at 535.5 cm^{-1} (ν_{32}) at ambient temperatures. This mode is related predominantly to the bending motion of the Si perpendicular the face joined by adjacent bridging (two O3) and non-bridging (O2) oxygens. Ultimately, this vibrational mode can be correlated to the overall volume of the SiO_4 tetrahedron (Fig. 3b). In this case, a 1% volume change corresponds to a 1.9 shift in wavenumbers. Further generalization of these relationships may permit Raman spectroscopy to be used *in situ* to probe crystal chemical properties, especially, during chemical reactions (e.g. crystallization), where the origin of the vibrational mode is known.

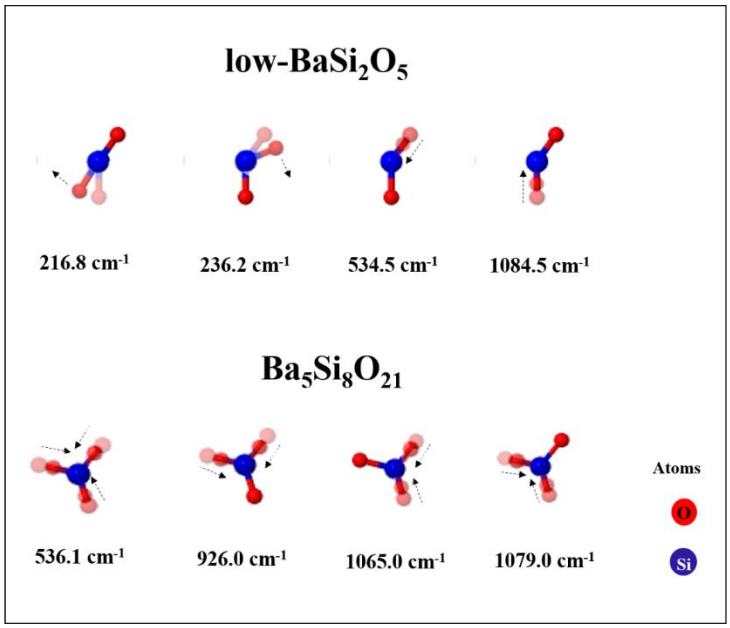

Figure 6. Vibrational modes of the tetrahedral group (SiO_4) for low-$BaSi_2O_5$: 216.8, 236.2, 534.5 and 1084.5 cm^{-1} and $Ba_5Si_8O_2$: 536.1, 926.0, 1065.0 and 1079.0 cm^{-1}.

The $Ba_5Si_8O_{21}$ spectra has a high number of vibrational modes which has the advantage of permitting quite well-constrained temperature dependence of the peak positions. However, the corollary is that this co-dependence becomes a disadvantage when one mode in a series of overlapping mode becomes poorly constrained such that it degrades the fit of all overlapping modes. Ultimately, of the 70 modes observed at ambient conditions, 28 were reliable characterized to temperatures above 800˚C (see Table 5). The temperature-dependent Raman study of the $Ba_5Si_8O_{21}$ was performed to obtain information on structural changes induced by temperature, and the wavenumber versus temperature plots are presented in Figure 7. We can observe that the Raman spectra remain nearly unchanged during the heating of the sample.

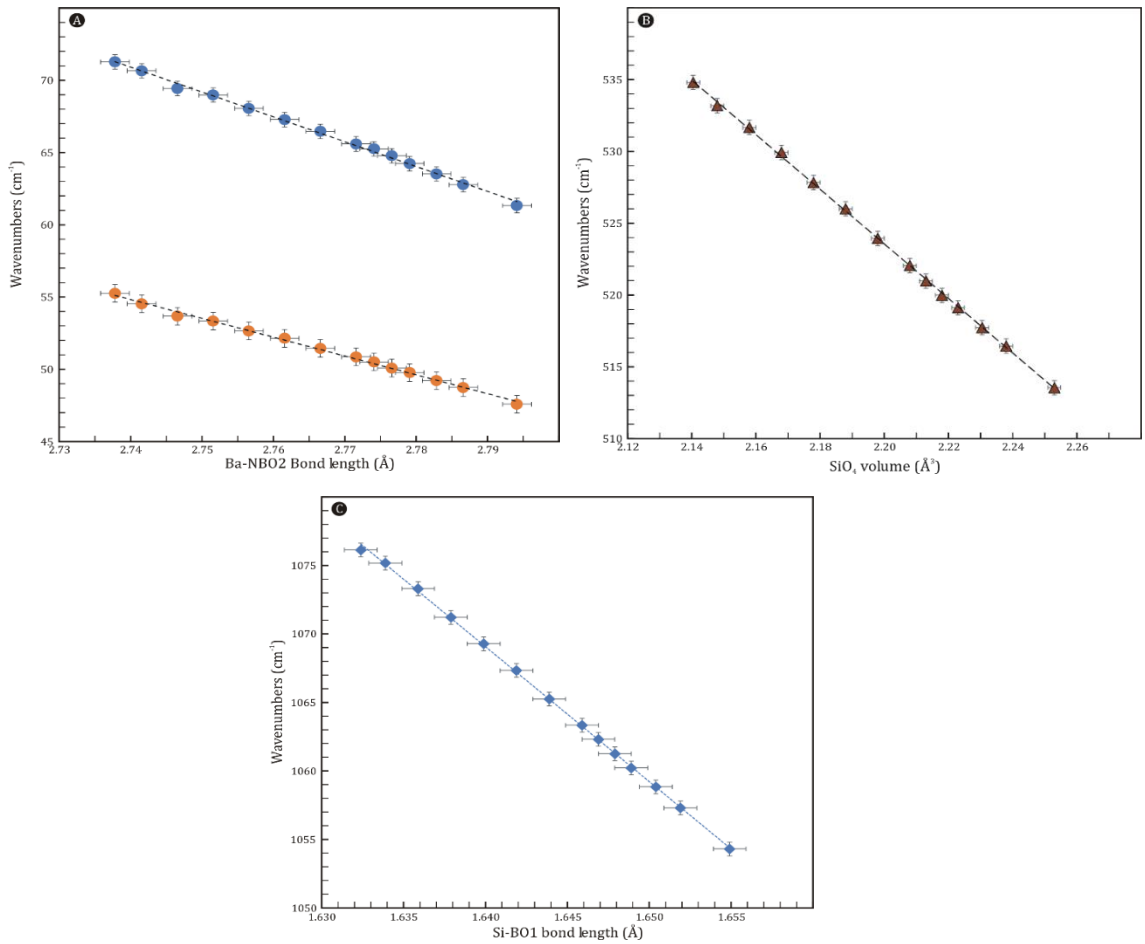

Figure 7. Frequency dependence on the bond length or tetrahedron volume derived from crystal structural parameters of low-$BaSi_2O_5$ determined to 1100˚C.
A) Shows the Ba-O2 vibrational modes at 55.0 ($v_1 = -130.4(d_{Ba-NBO}) + 411.5$, R^2 = 0.9968) and 71.9 cm^{-1} ($v_3 = -172.1(d_{Ba-NBO}) + 541.6$, R^2 = 0.9972). B) Shows the 535.5 cm^{-1} bending mode versus SiO_4 volume ($v_{32} = -190.1(SiO_4\ volume) + 941.8$, R^2 = 0.9995). C) Shows the 1077.9 cm^{-1} versus Si-O1 bond length ($v_{45} = -984.4(d_{Si-O1}) + 2683.5$, R^2 = 0.9995).

Notable among these modes are those that are similar to those in sanbornite, specifically those centered at 57, ~500, 900-1070 cm^{-1}, which are related to Si-O-Ba bending, and Ba-O and Si-O stretching motions, respectively. Unlike sanbornite, $Ba_5Si_8O_{21}$ does not have modes predominantly associated with specific Ba-oxygen bonding. The mode at 56.6 cm^{-1} (ν_2) involves rigid motion of the Ba2 site combined with the two opposing oxygens, O2 and O10, on adjacent tetrahedral ribbons. The linear correlation to the Ba2-O* distance is weaker (Fig. 8a) than observed for sanbornite (Fig. 6a). This is explained by the overlap of ν_2 mode with adjacent ν_1 and ν_3 modes. Likewise, the remaining modes involve more than one oxygen and often both Si and Ba. For

instance, the bending modes at 468.5 (ν_{59}) and 501.8 cm^{-1} (ν_{62}) involve Si4-O10-Ba2 and Si3-O6-Ba2, respectively (Table 3). Both should therefore be sensitive to the twisting of the adjacent tetrahedra with thermal expansion which is concentrated along the ribbon length rather than perpendicular to it [15]. Figure 8b shows the frequency dependence of these modes correlated to their respective Si-O and Ba-O bond lengths. They show excellent correlation in either case. This change is significant, because often shifts in bending modes are associated with changes in bond angles, however, in this case, the Si4-O10-Ba2 and Si3-O6-Ba2 angles change less than 1 degree between room temperature and 1000˚C, whereas these modes show large frequency displacements, both approximately -1 cm^{-1} for every 100˚C. These bending mode correlations are stronger than recent correlations found for orthoenstatite [29]. Ultimately, however, knowing the pressure dependence as well as the temperature dependence reported here would provide a more rigorous understanding of the volume dependence and consequently the thermodynamics of these phases.

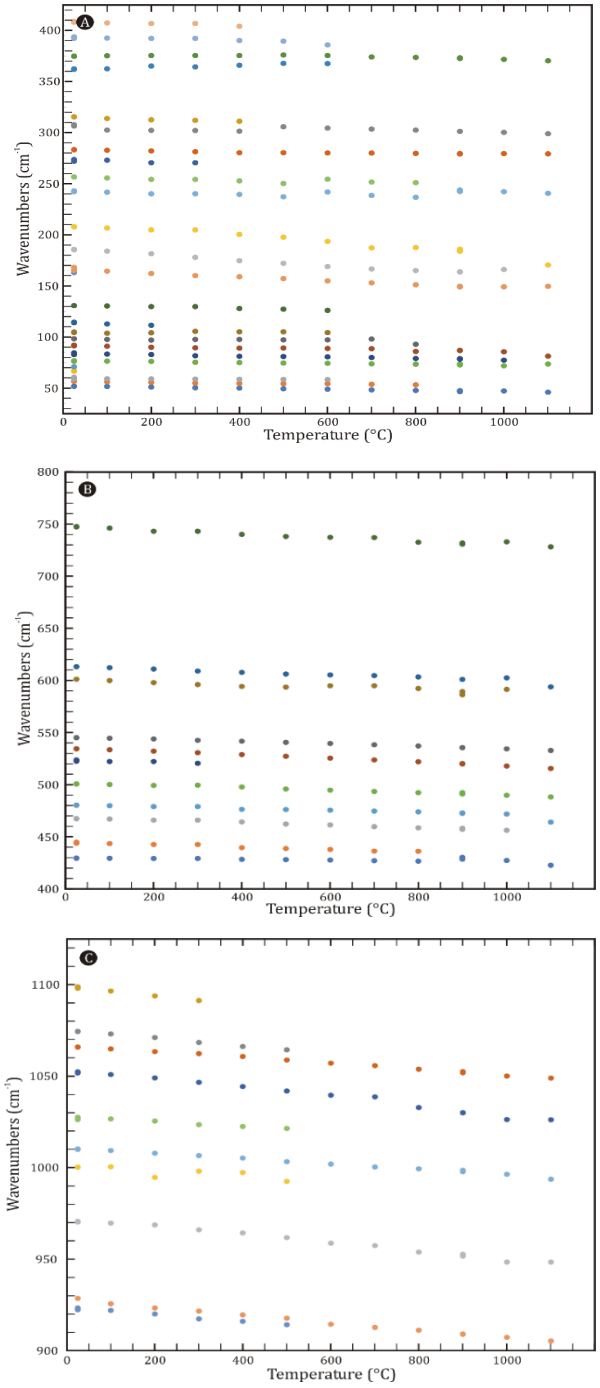

Figure 8: Temperature dependence of vibrational modes for $Ba_5Si_8O_{21}$ highlighting the A) low frequency, B) middle frequency, and C) high frequency mode behavior.

Finally, the stretching modes at 928.1 (ν_{83}) and 1066.6 (ν_{95}) cm^{-1} are uniquely associated with the Si1 (Q^2) and adjacent Si2 (Q^3) sites, respectively, and clearly persist to the highest temperatures investigated here (Fig. 4, 7). The Si1 mode involves both stretching of both adjacent oxygens, O1 and O2, away from the central silicon, whereas, the Si2 mode localized to the O5-Si2 bond. Both of these peaks overlap with adjacent modes although the ν_{95} mode suffers more from this issue. The high frequency B_g modes are quite sensitive to orientation, however, as this experiment was conducted on the same site, we can be certain that the same ν_{95} mode was followed throughout our high-temperature experiment. In the Si1 case, the average of the short, Si1-O1, and the long, Si1-O2, bond lengths are plotted against the frequency shift (Figure 8c). The strong correlations in both the peak center and linewidth affirm this interpretation (Table 5). In both cases, there is a strong correlation between the bond length and the frequency of these modes. Although not identical, nor should they be expected to be identical, they are similar. They indicate that a 0.01 Å change in bond length corresponds to a shift of 10 ± 2 cm^{-1}.

Table 5: Values of thermal effects on the mode parameters for $Ba_5Si_8O_{21}$*

Mode	Center (C)		Shift	Linewidth		% of Variance		γ_P[1]
	ν_0	T_{max}	$10^3\ \delta\nu/\delta T$	W_0	$10^3\ \delta W/\delta T$	ν	W	
ν_1	52.0	1100	-5.3	1.5	5.7	h	h	3.80
ν_2	56.6	800	-4.3	2.4	4.3	h	vl	2.83
ν_6	76.6	1100	-3.8	2.7	5.3	m	m	1.85
ν_{10}	83.9	1000	-6	5.8	3.5	h	m	2.66
ν_{12}	92.0	1100	-6.9	4	8.2	m	m	2.79
ν_{13}	98.0	800	-1.8	4.2	7.5	l	l	0.68
ν_{15}	104.5	600	0.8	6.2	n.d.	m	l	-0.29
ν_{19}	131.3	600	-8.1	5	n.d.	h	l	2.30
ν_{26}	166.3	1100	-17.8	12	n.d.	h	l	3.99
ν_{27}	185.4	1000	-23.9	13.8	13.8	h	l	4.80
ν_{29}	211.1	1000	-31.3	9.7	27.4	h	h	5.53
ν_{34}	241.0	1100	-0.4	10.7	29.2	vl	h	0.06
ν_{36}	256.2	800	-6.8	10.5	23.8	l	m	0.99
ν_{39}	282.8	1100	-3.8	8.2	24.8	m	vh	0.50
ν_{41}	305.3	1100	-4.5	9.9	18.1	vl	m	0.55
ν_{42}	315.4	400	-11.3	7.1	20.6	h	h	1.34
ν_{48}	362.0	600	10.1	4.9	8.3	h	l	-1.04
ν_{49}	376.0	1100	-3.6	5.9	19.3	l	m	0.36
ν_{51}	393.9	600	-10.4	7.9	17.7	m	h	0.98
ν_{54}	430.2	1100	-3.3	3.8	11.9	vl	m	0.29
ν_{57}	445.1	800	-11.5	9	8.4	h	l	0.96
ν_{59}	468.5	1000	-11.8	3.1	17	h	h	0.94
ν_{61}	481.6	1100	-11	4.9	19.3	m	h	0.85
ν_{62}	501.8	1100	-11.4	7.3	19.6	h	h	0.85
ν_{66}	535.6	1100	-17.2	6.6	16.2	vh	vh	1.20
ν_{68}	546.0	1100	-11.3	3.9	24.8	vh	vh	0.77
ν_{71}	600.8	1000	-11.8	5	19	m	h	0.73
ν_{72}	613.8	1100	-14.3	8.2	13.8	h	m	0.87
ν_{82}	923.6	500	-18.7	6.2	12.6	h	h	0.75
ν_{83}	928.1	1100	-21	6.5	19.7	vh	h	0.84
ν_{86}	972.2	1100	-22	9.9	23.2	h	h	0.84
ν_{89}	1010.8	1100	-14.5	2.1	27.9	vh	h	0.53
ν_{91}	1027.5	500	-12	6.8	28.5	h	m	0.44
ν_{93}	1053.8	1100	-25.4	4.6	34.2	h	l	0.90
ν_{95}	1066.6	1100	-16.0	5.6	18	vh	vh	0.56
ν_{96}	1075.1	500	-21.6	4.7	4.5	vh	l	0.75

* Parameters described as in table 4.

[1] isobaric mode-Grüneisen parameter calculated using α, the room temperature volume expansion coefficient, determined as 2.68×10^{-5}/K from the structural data of [15].

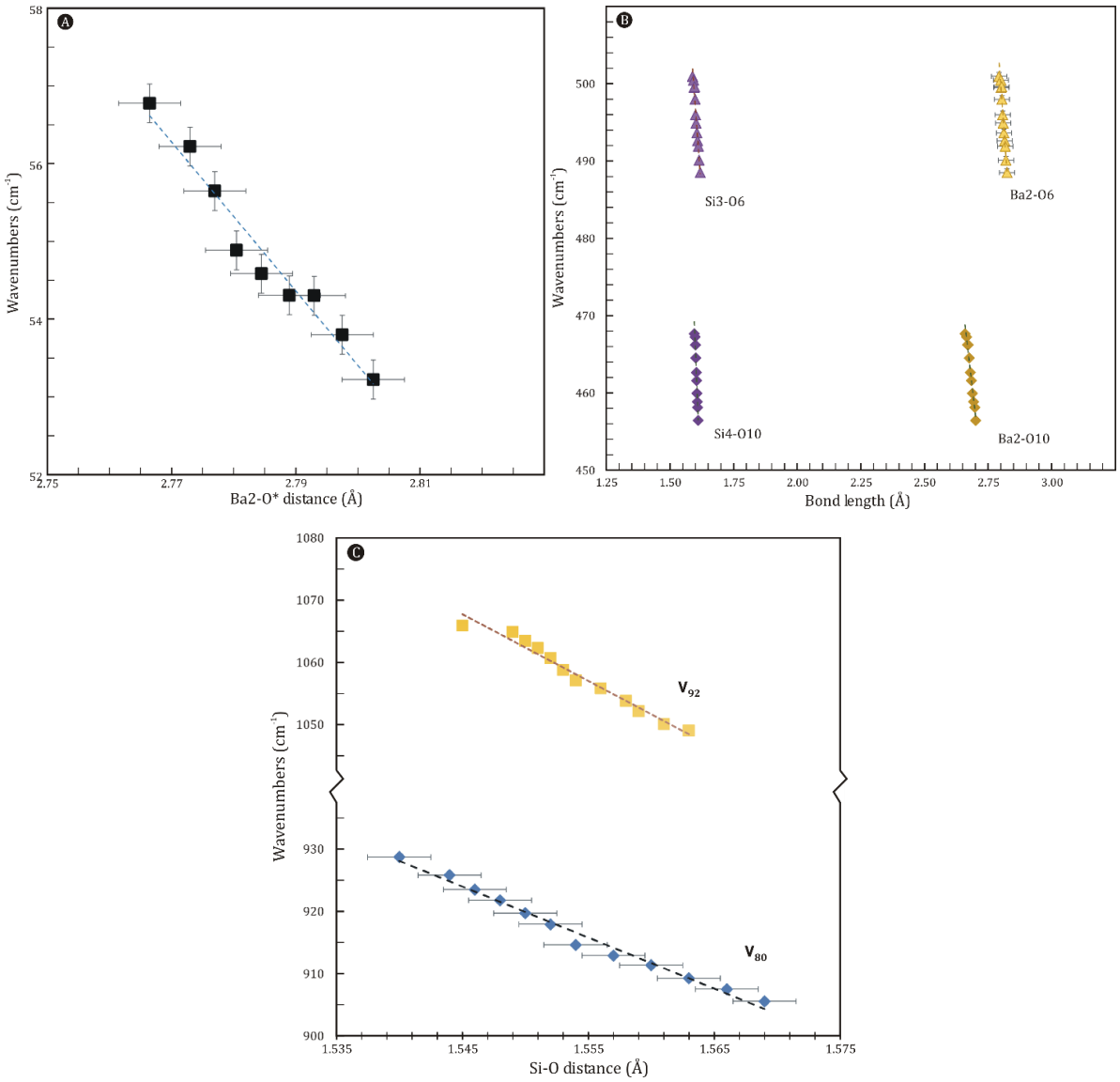

Figure 8: $Ba_5Si_8O_{21}$ frequency dependence of the crystal chemical parameters. A) frequency υ_2 versus Ba2-O* length, where O* is the mean bond lengths to the two oxygens (O6 and O10) involved in this motion. The dependence is described as -95.7(Ba-O) + 321.5 (R^2 = 0.96). B) Comparison of the mode shift to the Si-O and Ba-O bond lengths involved in the 468.5 cm^{-1} (ν_{59}) and 501.8 cm^{-1} (ν_{62}). (R^2 = 0.96-0.98). C) The Si-O stretching frequencies versus bond lengths for the Si1 at 928.1 cm^{-1} (ν_{83}) and the main Si2 band at 1066.6 cm^{-1} (ν_{95}).

363

364

365

366

6. Conclusions

The prominent phases of silicate: sanbornite and $Ba_5Si_8O_{21}$ have become ever more important for industrial applications and hold promise in understanding crystal nucleation and growth processes. Though widely used, Raman spectroscopy remains limited by an inability to make detailed mode assignments and consequently, clear and confident interpretations remain few and far between. This issue is largely overcome with *ab initio* calculations of vibrational frequencies, as done here. The vibrational mode assignments and their relation to the structural features has been reported in detail for both sanbornite and $Ba_5Si_8O_{21}$.

In addition, we report the temperature dependence of the Raman modes. Given the detailed mode assignments, associated to specific Ba or Si sites or bonding configurations have been revealed. Several examples, particularly of the stretching modes which are localized to specific Si-O bonds show strong correlations with the bond length changes up to 1100˚C. These relationships should be pursued to high pressures so that a complete thermodynamic model can be made. Finally, if the frequency dependence on some of these crystal chemical parameters can be generalized more broadly, *in situ* Raman experiments may lead to critical insights into *in situ* reactions, including crystallization and catalysis. Finally, we hope that this type of research can be considered a clear example of how the joint use of first principle calculations and experimental measurements of vibrational modes is an appropriate strategy to disclose the structure of complex oxide-based materials.

Acknowledgements

EOG acknowledges Generalitat Valenciana for the Santiago Grisolia program (2018/064). EOG and JA acknowledge financial support from Universitat Jaume I, for project UJI-B2019-30, and Ministerio de Ciencia, Innovación y Universidades (Spain) project PGC2018-094417-B-I00. We also wish to thank the Servei d'Informática, Universitat Jaume I, for their generous allocation of computer time. BJAM and TRC thank the São Paulo Research Foundation (FAPESP) for funding through grant numbers 2016/18567-5 and 2019/12383-8. PSP appreciates the support of CNPq and CAPES. We especially thank FAPESP for the CEPID project funding (no. 2013/07793-6) which made this a reality. Finally, we are thankful to Valmor Mastelaro for making this collaboration possible.

References

[1] R. Trejo, E. Lara-Curzio, A. Shyam, M.J. Kirkham, V. Garcia-Negron, Y. Wang, Physical and Mechanical Properties of Barium Alkali Silicate Glasses for SOFC Sealing Applications, Int. J. Appl. Glas. Sci. 3 (2012) 369–379. doi:10.1111/ijag.12004.

[2] J.H. Park, J.S. Kim, J.T. Kim, Luminescent properties of $BaSi_2O_5:Eu^{2+}$ phosphor film fabricated by spin-coating of Ba-Eu precursor on SiO_2 glass, J. Opt. Soc. Korea. 18 (2014) 45–49. doi:10.3807/JOSK.2014.18.1.045.

[3] F. Xiao, Y.N. Xue, Q.Y. Zhang, Bluish-green color emitting $Ba_2Si_3O_8:Eu^{2+}$ ceramic phosphors for white light-emitting diodes, Spectrochim. Acta - Part A Mol. Biomol. Spectrosc. 74 (2009) 758–760. doi:10.1016/j.saa.2009.08.011.

[4] M. Zhang, J. Wang, Q. Zhang, W. Ding, Q. Su, Optical properties of $Ba_2SiO_4:Eu^{2+}$ phosphor for green light-emitting diode (LED), Mater. Res. Bull. 42 (2007) 33–39. doi:10.1016/j.materresbull.2006.05.011.

[5] M. Kerstan, C. Rüssel, Barium silicates as high thermal expansion seals for solid

oxide fuel cells studied by high-temperature X-ray diffraction (HT-XRD), J. Power Sources. 196 (2011) 7578–7584. doi:10.1016/j.jpowsour.2011.04.035.

[6] S. Lin, H. Lin, Q. Huang, Y. Cheng, J. Xu, J. Wang, X. Xiang, C. Wang, L. Zhang, Y. Wang, A Photostimulated $BaSi_2O_5$:Eu^{2+} ,Nd^{3+} Phosphor-in-Glass for Erasable-Rewritable Optical Storage Medium, Laser Photon. Rev. 13 (2019) 1900006. doi:10.1002/lpor.201900006.

[7] J.K. Park, M.A. Lim, K.J. Choi, C.H. Kim, Luminescence characteristics of yellow emitting Ba_3SiO_5:Eu^{2+} phosphor, J. Mater. Sci. 40 (2005) 2069–2071. doi:10.1007/s10853-005-1237-z.

[8] R.M. Douglass, The crystal structure of sanbornite, $BaSi_2O_5$, Am. Mineral. 43 (1958) 517–536.

[9] R.E. Walstrom, J.F. Leising, Barium minerals of the Sanbornite Deposits, Axis. 1 (2005) 1–18. www.mineralogicalrecord.com.

[10] L.C. Basciano, L.A. Groat, A.C. Roberts, J.D. Grice, G.E. Dunning, E.E. Foord, I.M. Kjarsgaard, R.E. Walstrom, Kampfite, a new barium silicate carbonate mineral species from Fresno County, California, Can. Mineral. 39 (2001) 1053–1058. doi:10.2113/gscanmin.39.4.1053.

[11] K.F. Hesse, F. Liebau, Crystal chemistry of silica-rich Barium silicates I: Refinement of the crystal structures of $Ba_4[Si_6O_{16}]$, $Ba_5[Si_8O_{21}]$ and $Ba_6[Si_{10}O_{26}]$, silicates with triple, quadruple and quintuple chains, Zeitschrift Fur Krist. - New Cryst. Struct. 153 (1980) 3–17. doi:10.1524/zkri.1980.0002.

[12] K.F. Hesse, F. Liebau, Crystal chemistry of silica-rich Barium silicates III: Refinement of the crystal structures of the layer silicates $Ba_2[Si_4O_{10}]$ (I), (Sanbornite), and $Ba_2[Si_4O_{10}]$ (h), Zeitschrift Fur Krist. - New Cryst. Struct. 153 (1980) 33–41. doi:10.1524/zkri.1980.0004.

[13] F. Liebau, Structural Chemistry of Silicates, 1st ed., Springer Berlin Heidelberg,

448 Berlin, Heidelberg, 1985. doi:10.1007/978-3-642-50076-3.

449 [14] M. Czank, P.R. Buseck, Crystal chemistry of silica-rich barium silicates, Zeitschrift
450 Für Krist. - Cryst. Mater. 153 (1980) 19–32. doi:10.1524/zkri.1980.0003.

451 [15] L.A. Gorelova, R.S. Bubnova, S. V. Krivovichev, M.G. Krzhizhanovskaya, S.K.
452 Filatov, Thermal expansion and structural complexity of Ba silicates with
453 tetrahedrally coordinated Si atoms, J. Solid State Chem. 235 (2016) 76–84.
454 doi:10.1016/j.jssc.2015.12.012.

455 [16] S. Sen, T. Mukerji, A generalized classical nucleation theory for rough interfaces:
456 Application in the analysis of homogeneous nucleation in silicate liquids, J. Non.
457 Cryst. Solids. 246 (1999) 229–239. doi:10.1016/S0022-3093(99)00093-9.

458 [17] A.M. Rodrigues, D.R. Cassar, V.M. Fokin, E.D. Zanotto, Crystal growth and
459 viscous flow in barium disilicate glass, J. Non. Cryst. Solids. 479 (2018) 55–61.
460 doi:10.1016/j.jnoncrysol.2017.10.007.

461 [18] V.M. Fokin, E.D. Zanotto, N.S. Yuritsyn, J.W.P. Schmelzer, Homogeneous crystal
462 nucleation in silicate glasses: A 40 years perspective, J. Non. Cryst. Solids. 352
463 (2006) 2681–2714. doi:10.1016/j.jnoncrysol.2006.02.074.

464 [19] X. Xia, I. Dutta, J.C. Mauro, B.G. Aitken, K.F. Kelton, Temperature dependence of
465 crystal nucleation in $BaO \cdot 2SiO_2$ and $5BaO \cdot 8SiO_2$ glasses using differential thermal
466 analysis, J. Non. Cryst. Solids. 459 (2017) 45–50.
467 doi:10.1016/j.jnoncrysol.2016.12.032.

468 [20] L. Cai, R.E. Youngman, D.E. Baker, A. Rezikyan, M. Zhang, B. Wheaton, I. Dutta,
469 B.G. Aitken, A.J. Allen, Nucleation and early stage crystallization in barium
470 disilicate glass, J. Non. Cryst. Solids. 548 (2020) 120330.
471 doi:10.1016/j.jnoncrysol.2020.120330.

472 [21] Y. Takahashi, M. Osada, H. Masai, T. Fujiwara, Structural heterogeneity and
473 homogeneous nucleation of $1BaO\text{-}2SiO_2$ glass, Appl. Phys. Lett. 94 (2009) 211907.

474 doi:10.1063/1.3142394.

475 [22] E.D. Zanotto, P.F. James, Experimental test of the general theory of
476 transformation kinetics: Homogeneous nucleation in a $BaO \cdot 2SiO_2$ glass, J. Non.
477 Cryst. Solids. 104 (1988) 70–72. doi:10.1016/0022-3093(88)90183-4.

478 [23] A. Herrmann, A. Simon, C. Rüssel, Preparation and luminescence properties of
479 Eu2-doped $BaSi_2O_5$ glass-ceramics, J. Lumin. 132 (2012) 215–219.
480 doi:10.1016/j.jlumin.2011.08.024.

481 [24] P. Wang, X. Xu, D. Zhou, X. Yu, J. Qiu, Sunlight Activated Long-Lasting
482 Luminescence from $Ba_5Si_8O_{21}:Eu^{2+},Dy^{3+}$ Phosphor, Inorg. Chem. 54 (2015) 1690–
483 1697. doi:10.1021/ic5026312.

484 [25] Y. Takahashi, H. Masai, M. Osada, R. Ihara, T. Fujiwara, Formation of spherulite
485 and metastable phase in stoichiometric $Ba_2Si_3O_8$ glass, J. Ceram. Soc. Japan. 118
486 (2010) 955–958. doi:10.2109/jcersj2.118.955.

487 [26] B.J.A. Moulton, A.M. Rodrigues, P.S. Pizani, D.V. Sampaio, E.D. Zanotto, A
488 Raman investigation of the structural evolution of supercooled liquid barium
489 disilicate during crystallization, Int. J. Appl. Glas. Sci. 9 (2018) 510–517.
490 doi:10.1111/ijag.12356.

491 [27] B.J.A. Moulton, A.M. Rodrigues, D. V. Sampaio, L.D. Silva, T.R. Cunha, E.D.
492 Zanotto, P.S. Pizani, The origin of the unusual DSC peaks of supercooled barium
493 disilicate liquid, CrystEngComm. 21 (2019) 2768–2778. doi:10.1039/c8ce02054j.

494 [28] L.L. Evaristo, B.J.A. Moulton, P.S. Pizani, S. Buchner, Effect of high pressure on
495 the structure of barium disilicate glass-ceramics, J. Non. Cryst. Solids. 550 (2020)
496 120380. doi:10.1016/j.jnoncrysol.2020.120380.

497 [29] C. Stangarone, M. Tribaudino, M. Prencipe, P.P. Lottici, Raman modes in Pbca
498 enstatite ($Mg_2Si_2O_6$): an assignment by quantum mechanical calculation to
499 interpret experimental results, J. Raman Spectrosc. 47 (2016) 1247–1258.

doi:10.1002/jrs.4942.

[30] C. Stangarone, U. Böttger, D. Bersani, M. Tribaudino, M. Prencipe, Ab initio simulations and experimental Raman spectra of Mg_2SiO_4 forsterite to simulate Mars surface environmental conditions, J. Raman Spectrosc. 48 (2017) 1528–1535. doi:10.1002/jrs.5127.

[31] A. Wang, B.L. Jolliff, L.A. Haskin, K.E. Kuebler, K.M. Viskupic, Characterization and comparison of structural and compositional features of planetary quadrilateral pyroxenes by Raman spectroscopy, Am. Mineral. 86 (2001) 790–806. doi:10.2138/am-2001-0703.

[32] H.M. Rietveld, Line profiles of neutron powder-diffraction peaks for structure refinement, Acta Crystallogr. 22 (1967) 151–152. doi:10.1107/S0365110X67000234.

[33] A.C. Larson, R.B. Von Dreele, General Structure Analysis System (GSAS), Los Alamos Natl. Lab. Rep. LAUR. 748 (2004) 86–748. doi:10.1103/PhysRevLett.101.107006.

[34] R. Dovesi, A. Erba, R. Orlando, C.M. Zicovich-Wilson, B. Civalleri, L. Maschio, M. Rérat, S. Casassa, J. Baima, S. Salustro, B. Kirtman, Quantum-mechanical condensed matter simulations with CRYSTAL, Wiley Interdiscip. Rev. Comput. Mol. Sci. 8 (2018) e1360. doi:10.1002/wcms.1360.

[35] M.D. Towler, BARIUM BASIS SETS FOR THE CRYSTAL PROGRAM, (1996). https://vallico.net/mike_towler//basis_sets/Ba_basis.txt.

[36] R. Nada, J.B. Nicholas, M.I. McCarthy, A.C. Hess, Basis sets for ab initio periodic Hartree—Fock studies of zeolite/adsorbate interactions: He, Ne, and Ar in silica sodalite, Int. J. Quantum Chem. 60 (1996) 809–820. doi:10.1002/(SICI)1097-461X(1996)60:4<809::AID-QUA3>3.3.CO;2-F.

[37] L. Valenzano, F.J. Torres, K. Doll, F. Pascale, C.M. Zicovich-Wilson, R. Dovesi, Ab Initio Study of the Vibrational Spectrum and Related Properties of Crystalline

526 Compounds; the Case of CaCO3 Calcite, Zeitschrift Für Phys. Chemie. 220 (2006)
527 893–912. doi:10.1524/zpch.2006.220.7.893.

528 [38] L.B. McCusker, R.B. Von Dreele, D.E. Cox, D. Louër, P. Scardi, Rietveld
529 refinement guidelines, J. Appl. Crystallogr. 32 (1999) 36–50.
530 doi:10.1107/S0021889898009856.

531 [39] F.C. Hawthorne, Y.A. Uvarova, E. Sokolova, A structure hierarchy for silicate
532 minerals: sheet silicates, Mineral. Mag. 83 (2019) 3–55. doi:10.1180/mgm.2018.152.

533 [40] M.C. Day, F.C. Hawthorne, A structure hierarchy for silicate minerals: chain,
534 ribbon, and tube silicates, Mineral. Mag. 84 (2020) 165–244.
535 doi:10.1180/mgm.2020.13.

536 [41] W.G. Fateley, F.R. Dollish, N.T. McDevitt, F.F. Bentley, Infrared and Raman
537 Selection Rules for Lattice Vibrations: The Correlation Method, John Wiley &
538 Sons, Inc., Toronto, 1972.

539 [42] Y. Takahashi, R. Ihara, T. Fujiwara, M. Osada, Crystallization and Morphology of
540 Glassy Sanbornite, Key Eng. Mater. 485 (2011) 301–304.
541 doi:10.4028/www.scientific.net/KEM.485.301.

542

543

544